Wireless Power Transfer

ARTICLE

Open Access

https://doi.org/10.48130/wpt-0025-0013

Wireless Power Transfer **2025**, 12: e019

Improving misalignment tolerance for a third coil IPT charger with load-independent output

Hailong Zhang, Shuo Tian, Helin Wang and Xiaoyan Zhou*

Department of Information and Control Engineering, Qingdao University of Technology, Qingdao 266525, China

* Corresponding author, E-mail: zxy021678@163.com

Abstract

This paper proposes a system to improve misalignment tolerance and achieve constant current (CC) and constant voltage (CV) outputs for an electric bicycle inductive power transfer (IPT) charger. Existing systems typically sacrifice output stability when enhancing misalignment tolerance and often rely on complex control circuits for CC-CV switching. A tertiary coil is utilized to establish a reverse connection with the secondary side coil without affecting the inherent output characteristics. The loosely coupled transformer with a third coil can effectively improve the misalignment tolerance in the x- and y-directions. In addition, a simple and reconfigurable structure is developed, enabling shifts from inductor-capacitor-capacitor-inductor-capacitor-capacitor (LCC-LCC) topology to inductor-capacitor-capacitor-series (LCC-S) topology, and further acquiring load-independent CC and CV outputs. The proposed tri-coil design simultaneously addresses misalignment challenges while eliminating control complexity. JMAG simulation and experimental findings confirm the accuracy of the suggested model and its structural design. The experimental results show that the prototype achieves an output power of 200 W with a maximum efficiency of 92.7%.

Citation: Zhang H, Tian S, Wang H, Zhou X. 2025. Improving misalignment tolerance for a third coil IPT charger with load-independent output. *Wireless Power Transfer* 12: e019 https://doi.org/10.48130/wpt-0025-0013

Introduction

Electric bicycles are usually equipped with electric motors for propulsion and battery packs to power the motors. In this context, the traditional way of wired charging requires that the bike be connected directly to the charger or that the heavy on-board battery pack be removed for connection to the charger. Inductive power transfer (IPT) systems can be applied to achieve a non-contact power supply, which makes them robust to dirt, ice, water, and chemicals, thus eliminating the need for maintenance.

An excellent anti-misalignment performance plays a vitally important role in the wireless charging system for electric bicycles. At the receiving end of an electric bicycle, there is an offset of horizontal position during placement, which affects the coupling coefficient of the wireless charging system, thus reducing both output power and efficiency.

Many studies have been conducted to enhance the misalignment features of wireless power transfer (WPT) systems. For instance, a detuning compensation network has been proposed to study and enhance the misalignment performance[1]. To enhance the misalignment performance, the transmitting resonator and the receiving resonator are adjusted to be inductive and capacitive at the operating frequency, respectively[2]. Both S/SP compensation and PS/S compensation are proposed as a general method that can be used to develop the primary compensation network for dynamic WPT systems[3,4]. Utilizing this technique, a T-type compensation network has been created for dynamic WPT systems. Additionally, a primary-side X-type compensation topology for WPT systems has been proposed to achieve stable output in the presence of misalignment[5].

The methods for controlling misalignment tolerance have been thoroughly studied[6–8]. These methods usually require the use of communication devices, which tend to induce data latency. Moreover, the controllers can be disrupted by extra volume and complex control circuits.

Simplification of control strategies is possible if IPT systems can withstand misalignment. Consequently, scientists are concentrating on improving misalignment tolerance by designing magnetic pads, fine-tuning compensation settings, and creating hybrid structures. For example, double-D, dipole, tripole pads, and asymmetric magnetic couplers, have been proposed to generate a relatively uniform magnetic field[9–12]. However, some methods are applicable only when the operation is conducted with misalignment tolerance in one direction. Additionally, there is minimal focus on examining the steady output traits of these IPT systems.

A hybrid WPT system is presented to perform CC-CV output charging with a high misalignment tolerance for charging EV batteries[13]. The ZPA condition and ZVS soft switching are easily achievable throughout the charging process, even in the presence of misalignment. However, there is a high complexity in the coupling relationship of this model. The power density and system efficiency are decreased due to using multiple coils.

There are also examples of introducing DD coils and utilizing dual receivers with DD and Q coils to improve misalignment performance[14]. The DD and Q coils are inherently separated. Nonetheless, it seems improbable that a pair of receiver coils will concurrently emit the identical magnetic field produced by the DD transmitter. Another option involves using the Q coil to overlap with the DD coil, where a compact double-sided decoupled-coil-based WPT system has been proposed[15]. The suggested design suggests a more intense magnetic field on one side of this coupler compared to the other, potentially leading to magnetic saturation.

In engineering works, IPT technology is applied primarily to the battery load. During the charging process, the equivalent impedance of the battery changes constantly[16]. Also, coil misalignment can reduce its coupling coefficient, resulting in a significant deviation from the rated duty point and a decline in efficiency of the system[17]. Environmental factors such as ocean currents can lead to coupler displacement during deep-sea charging operations, while terrestrial charging systems face similar challenges when vehicular

positioning errors exceed coil alignment tolerances. Therefore, the IPT system is required to achieve load-independent constant output and show strong robustness to coupling variation.

To achieve this purpose, various control methods such as phase-shift control, pulse frequency control, frequency control, and hybrid control methods have been proposed[18–21]. However, the use of complex control methods tends to increase the overall system cost and power loss. In addition, the stability of the control system can be affected by the speed and accuracy of data transmission.

Reconfigurable topology provides another solution to achieving the strong tolerance of misalignment. A reconfigurable series–series (SS) topology is presented to ensure the stability of output in the presence of significant coupling variation. However, low efficiency results from using a large number of composition components. To minimize the number of composition components used, a reconfigurable rectifier-based detuned SS topology is presented[22]. Nevertheless, the use of detectors and controllers is required to enable the reconfiguration, which remains an issue with the control strategy.

A bicycle inductive power transfer system should meet the following requirements. one is to achieve misalignment tolerance in x- and y-directions; another is to improve battery life through CC and CV charging; the last one is a high power density of the system to meet the requirements for high integration and efficiency.

This paper aims to address the aforementioned problems by developing a wireless charging system with high misalignment tolerance and load-independent output. The secondary side utilizes thin magnetic materials without aluminium shielding. Furthermore, in the actual experimental process, the reconfigurable topology and related control circuits are integrated into the secondary side coil in order to further reduce the weight of the receiving end. According to the results of the JMAG simulation and experiment, the proposed model and the topology are effective. To be specific, the prototype output power reaches 200 W with a maximum efficiency of 92.7%.

Analysis of the IPT system with a third coil

The coil structure presented in this paper is in reverse parallel with the third coil on the secondary side, with a single coil on the primary side. The equivalent model of the coil is shown in Fig. 1.

The secondary side coil current I_s inflow from the secondary side coil L_s and exits through the third coil. L_T. L_P, L_S, and L_T are inductances of the primary, secondary, and auxiliary coils of the loosely coupled transformer. U_P, U_S, I_P, and I_S represent the input/output voltage and current of the coupler. M_{PT}, M_{PS}, and M_{TS} are the relevant coupling coefficients of the primary coil, secondary coil, and additional coil. According to the M model and Kirchhoff's law as shown in Fig. 2, it can be indicated that:

$$\begin{bmatrix} \dot{U}_P \\ \dot{U}_S \end{bmatrix} = \begin{bmatrix} j\omega L_P & j\omega(M_{PS}-M_{TS}) \\ j\omega(M_{PS}-M_{TS}) & j\omega(L_S+L_T-2M_{PT}) \end{bmatrix} \begin{bmatrix} \dot{I}_P \\ \dot{I}_S \end{bmatrix} \quad (1)$$

For convenience of analysis, the secondary side coil L_S and auxiliary coil L_T can be equivalent to one coil M_{EQ}. The relationship between self-inductance and mutual inductance in Fig. 3 is shown as follows:

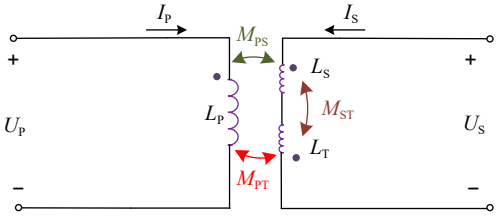

Fig. 1 Equivalent circuit of the proposed coil.

$$L_P' = L_P + L_T - 2M_{PT} \quad (2)$$

$$M_{EQ} = M_{PS} - M_{PT} \quad (3)$$

M_{PS} and M_{PT} are reduced simultaneously under the misalignment condition. The degree of reduction of the two mutual inductances is expressed as ΔM_{PS} and ΔM_{PT}. The equivalent mutual inductance coefficient can be expressed as:

$$\begin{aligned} M_{EQ}' &= (M_{PS} - \Delta M_{PS}) - (M_{TS} - \Delta M_{TS}) \\ &= M_{EQ} - (\Delta M_{PS} - \Delta M_{TS}) \end{aligned} \quad (4)$$

Assuming that $\Delta M_{PS} = \Delta M_{PT}$, then $M_{EQ}' = M_{EQ}$, it indicates that the mutual inductance remains stable under the misalignment condition. Therefore, the anti-misalignment characteristics of the proposed coil can be improved. Common resonant network topologies, such as SS, SP, LCL, and LCC, can be applied in the proposed loosely coupled transformer without affecting the output characteristics of the original topology. Mutual inductance M_{PS} and M_{PT} both decrease under the misalignment condition. The equivalent mutual inductance coefficient ($M_e = M_{PS} - M_{TS}$) remains stable, assuming that $\Delta M_{PS} = \Delta M_{PT}$. The output of the loosely coupled transformer (LCT) is not affected by the coupling variation, thus increasing the misalignment tolerance.

Theoretical analysis in the CV and CC mode

The circuit diagram of the proposed system is shown in Fig. 3. U_{AB} and I_{in} are the AC output voltage and current of the half-bridge inverter, and U_{ab} and I_{ab} represent the AC input voltage and current of the rectifier. U_{DC} and I_{DC} represent the DC input voltage and current of the half-bridge inverter, and U_b and I_b are the DC output voltage and current of the rectifier. The high-order compensation networks LCC, composed of L_1, C_{p1}, C_{f1}, and L_2, C_{p2}, C_{f2} are applied on the primary and secondary sides, respectively.

When the topology operates in CV mode, switch Q_4 is turned ON, and Q_3 and Q_5 are turned OFF, constructing LCC-S topology. The AC-DC rectifier is realized by a half-bridge on the secondary side. The reconfigurable topology and equivalent circuit for CV mode are presented in Figs 4 and 5. For Fig. 4, the current flows through freewheeling diode of Q_4 and diode D_6.

The Kirchhoff's law-based formula for the AC input current is:

$$I_{in} = \frac{U_{AB}}{Z_{in}} = \frac{U_{AB}M_{EQ}^2}{L_1{}^2 R_{ac}} \quad (5)$$

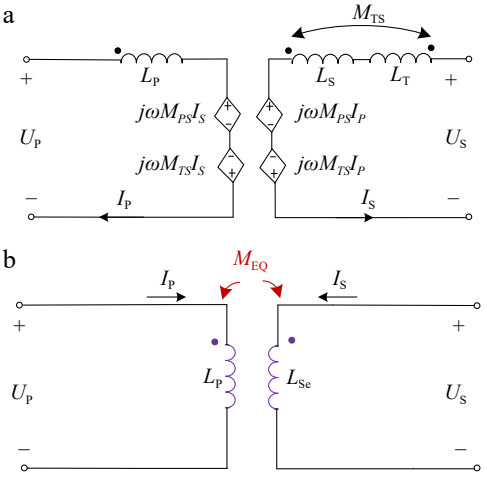

Fig. 2 M model and equivalent model of the proposed coil. (a) M model. (b) Equivalent model.

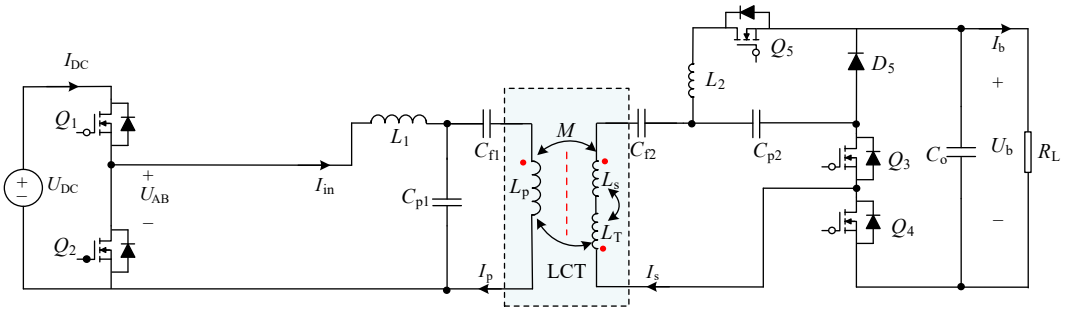

Fig. 3 Circuit diagram of the proposed system.

The AC output voltage and voltage gain ratio can be determined as:

$$\begin{cases} U_{ab} = I_s R_{ac} = \dfrac{M_{EQ} U_{AB}}{L_1} \\ G_V = \left| \dfrac{U_{ab}}{U_{AB}} \right| = \dfrac{M_{EQ}}{L_1} \end{cases} \tag{6}$$

The current on the primary and secondary side coils is derived as:

$$\begin{cases} I_p = \dfrac{R_{ac} U_{AB}}{(\omega_0 M_{EQ})^2} \\ I_s = \dfrac{M_{EQ} U_{AB}}{L_1 R_{ac}} \end{cases} \tag{7}$$

The DC output voltage and current can be calculated as:

$$\begin{cases} I_b = \dfrac{1}{2} \dfrac{M_{EQ} U_{AB}}{L_1 R_L} \\ U_b = \dfrac{1}{2} \dfrac{M_{EQ}}{L_1} U_{AB} \end{cases} \tag{8}$$

The input and output voltage and current relationship is given as:

$$\begin{cases} U_{AB} = \dfrac{\sqrt{2} U_{DC}}{\pi} \\ I_{in} = \dfrac{\sqrt{2} I_{DC}}{\pi} \end{cases} \tag{9}$$

$$\begin{cases} U_b = \dfrac{\sqrt{2} U_{ab}}{\pi} \\ I_b = \dfrac{\pi I_{ab}}{\sqrt{2}} \end{cases} \tag{10}$$

The relationship of AC and DC resistance is calculated as:

$$R_{ac} = \frac{2}{\pi^2} R_L \tag{11}$$

The calculated AC-AC efficiency can be derived as:

$$\eta = \frac{I_s^2 R_{ac}}{I_s^2 R_{ac} + I_{in}^2 R_{L1} + I_p^2 R_p + I_S^2 R_S} = \frac{1}{1 + \dfrac{R_S}{R_{ac}} + \dfrac{R_p R_{ac}}{(\omega_0 M_{EQ})^2} + \left(\dfrac{M_{EQ}}{L_1} \right)^2 \dfrac{R_{L1}}{R_{ac}}} \tag{12}$$

The optimal AC resistance is obtained by derivation as:

$$R_{ac} = \sqrt{\frac{R_S + \left(\dfrac{M}{L_1} \right)^2 R_{L1}}{R_p}} \omega_0 M_{EQ} \tag{13}$$

When the topology operates in CC mode, switches Q_3 and Q_5 are turned ON, and Q_4 is turned OFF, forming the LCC-LCC topology. The AC-DC rectifier is realized by a half-bridge on the secondary side. The reconfigurable topology and equivalent circuit for CC mode are presented in Figs 6 and 7. For Fig. 6; the current flows through the freewheeling diode of Q_4 and diode D_6.

The resonant conditions of the LCC-LCC topology can be given as:

$$\begin{aligned} &\omega_0^2 L_1 C_{P1} = \omega_0^2 L_2 C_{P2} = 1 \\ &\omega_0^2 (L_P - L_1) C_{f1} = \omega_0^2 (L_P - L_2) C_{f2} = 1 \end{aligned} \tag{14}$$

The AC input and output current can be calculated as:

$$\begin{cases} I_{in} = \dfrac{U_{AB} M^2 R_{ac}}{\omega_0^2 L_1^2 L_2^2} \\ I_o = \dfrac{M U_{AB}}{\omega_0 L_1 L_2} \end{cases} \tag{15}$$

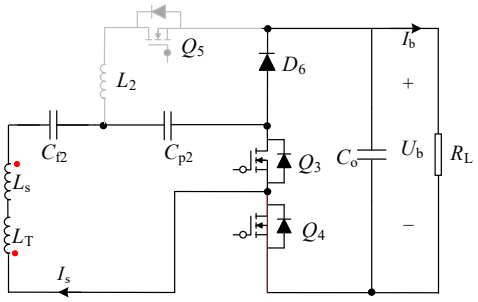

Fig. 4 Equivalent circuit in CV mode.

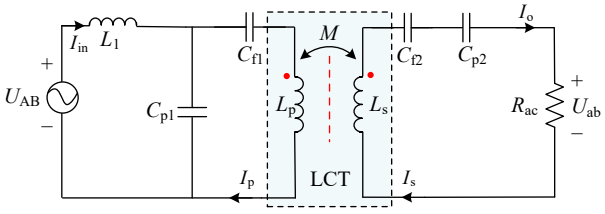

Fig. 5 Equivalent resonant network in CV mode.

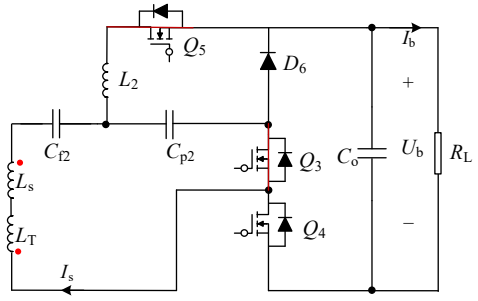

Fig. 6 Equivalent circuit in CC mode.

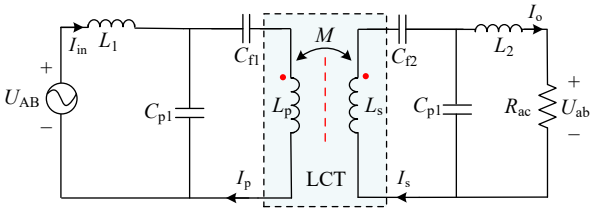

Fig. 7 Equivalent circuit of the proposed IPT system in CC mode.

The current on the primary side and secondary side coils is expressed as:

$$\begin{cases} I_{\mathrm{P}} = \dfrac{U_{\mathrm{AB}}}{\omega_0 L_1} \\ I_{\mathrm{S}} = \dfrac{M U_{\mathrm{AB}} R_{\mathrm{ac}}}{\omega_0^2 L_1 L_2^2} \end{cases} \tag{16}$$

The AC output current and voltage are given as:

$$\begin{cases} I_{\mathrm{o}} = \dfrac{M_{\mathrm{EQ}} U_{\mathrm{AB}}}{\omega_0 L_1 L_2} \\ U_{\mathrm{o}} = \dfrac{M U_{\mathrm{AB}} R_{\mathrm{ac}}}{\omega_0 L_1 L_2} \end{cases} \tag{17}$$

The DC output current and voltage are given as:

$$\begin{cases} I_{\mathrm{b}} = \dfrac{\pi M_{\mathrm{EQ}} U_{\mathrm{AB}}}{\sqrt{2}\omega_0 L_1 L_2} \\ U_{\mathrm{b}} = \dfrac{\sqrt{2} M_{\mathrm{EQ}} U_{\mathrm{AB}} R_{\mathrm{ac}}}{\pi \omega_0 L_1 L_2} \end{cases} \tag{18}$$

The output power can be calculated as:

$$P_{\mathrm{in}} = P_{\mathrm{O}} = \frac{U_{\mathrm{AB}}^2 M_{\mathrm{EQ}}^2 R_{\mathrm{ac}}}{\omega_0^2 L_1{}^2 L_2{}^2} \tag{19}$$

The calculated AC-AC efficiency can be derived as:

$$\eta = \frac{I_{\mathrm{s}}^2 R_{\mathrm{ac}}}{I_{\mathrm{S}}^2 R_{\mathrm{ac}} + I_{\mathrm{in}}^2 R_{\mathrm{L1}} + I_{\mathrm{p}}^2 R_{\mathrm{p}} + I_{\mathrm{S}}^2 R_{\mathrm{S}}} = \frac{1}{1 + \dfrac{R_{\mathrm{L1}}}{R_{\mathrm{ac}}}\left(\dfrac{M}{L_1}\right)^2 + \dfrac{R_{\mathrm{p}} \omega_0^2 L_2^4}{R_{\mathrm{ac}}^3 M_{\mathrm{EQ}}^2} + \dfrac{R_{\mathrm{S}}}{R_{\mathrm{ac}}}} \tag{20}$$

The optimal AC resistance is obtained by derivation as:

$$R_{\mathrm{ac}} = \sqrt{\frac{3M^2 R_{\mathrm{p}} \omega_0^2 L_1^4 L_2^2}{M_{\mathrm{EQ}}^6 L_1^2 R_{\mathrm{L1}} + R_{\mathrm{S}} M_{\mathrm{EQ}}^4 L_1^4}} \tag{21}$$

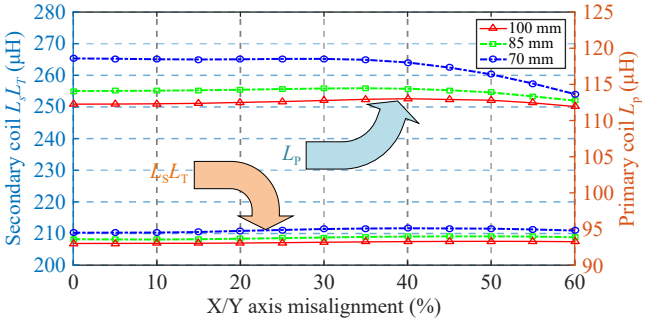

Fig. 8 Self-inductance change of the proposed three-coil structure.

Overall design process of the proposed system

As shown in Fig. 8, when the position is offset, the amplitude of change in the self-inductance of the single coil on the primary side is greater than on the secondary side, especially given a narrower air gap. It can be seen from Fig. 9 that in CC and CV modes, changes in the self-inductance value of the primary coil will not affect the current and voltage gains. Moreover, the input phase angle increases as the self-inductance value decreases, which will cause the input impedance of the system to exhibit inductive drift, causing the MOSFETs to operate under ZVS conditions. However, changes in the self-inductance value of the secondary side coil can have a significant impact on the current and voltage gains. Changes in the self-inductance value of the secondary side coil can significantly affect the magnitude of the current gain. In addition, the reduction in self-inductance value will cause the input impedance of the system to exhibit capacitive drift, thereby affecting the inverter's ability to achieve ZVS. Therefore, the third coil on the secondary side is more significant to the design of the compensation network at the receiving end, and the misalignment performance is also improved.

Figure 3 illustrates the circuit configuration of the proposed system, which consists of the three-coil magnetic coupling mechanism and reconfiguration rectifier topology. In this system, communication is not required between the primary and secondary sides. Based on the physical demand for electric bicycles, the third coil structure ($L_{\mathrm{P}} : L_{\mathrm{S}} : L_{\mathrm{T}}$) was designed as 240:250:160 mm to ensure that the constructed LCT exhibited effective misalignment tolerance capability in the x and y directions. In addition, the third coil effectively reduces the self-inductance variation under the misalignment condition on the secondary side. It should be noted that the designed LCT was not shielded with aluminium due to the low charging power of the electric bicycle.

The geometric configuration of electromagnetic couplers and their resonant frequency f_0 in IPT systems is predominantly governed by structural constraints and environmental deployment conditions, necessitating the predefinition of f_0 during initial parameter configuration. In the meantime, the radius R(P), the turns n_{p}, and the radius R(S), the number of turns n_{S}, n_{T}, are also decided by the application scenarios. Similarly, the wire diameter of Litz wire, the distance of the air gap, and the permeability, conductivity, thickness, length, and width of the ferrite core can be set according to actual needs. Magnetic ferrite was added to the primary side in order to reduce the weight of the receiving side. The design flowchart of the coupler is given in Fig. 10. The flowchart of design

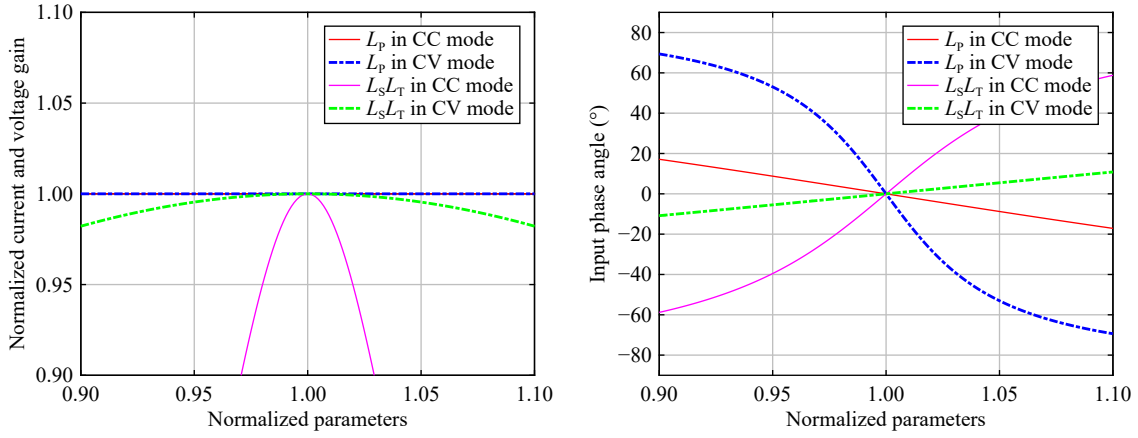

Fig. 9 Relationship curves between the normalized current/voltage gain and input phase angle with the normalized self-inductance value in CC mode and CV mode.

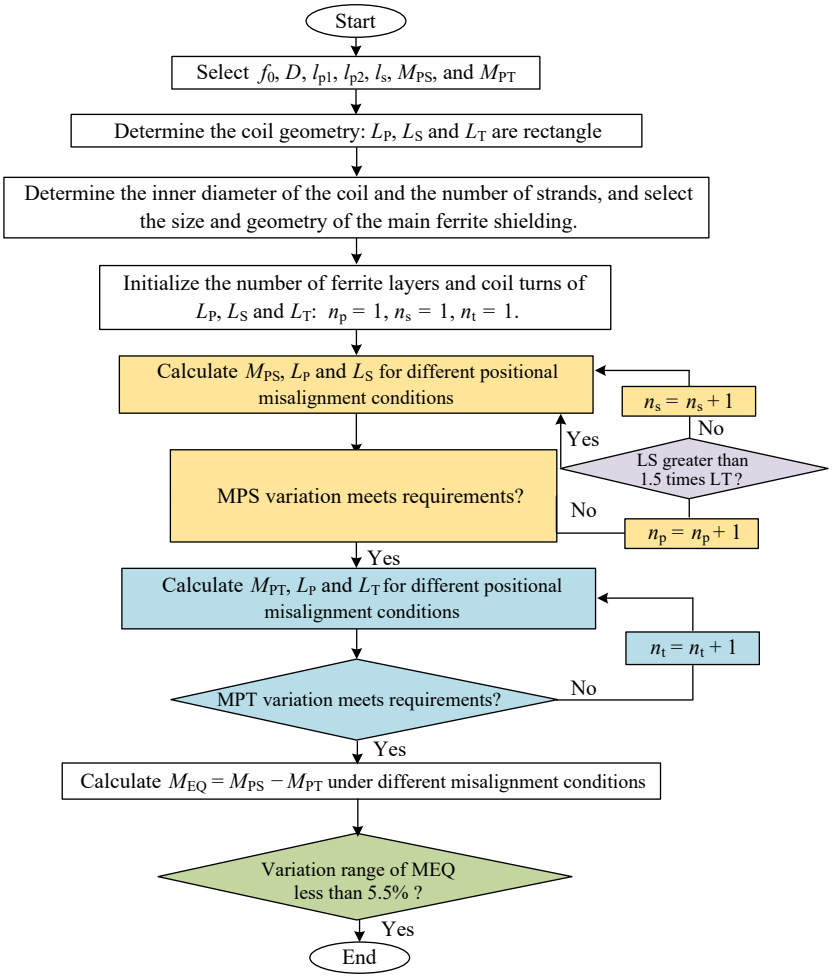

Fig. 10 Flow chart of the proposed coupler.

for the entire IPT system is shown in Fig. 11. Firstly, the initial parameter values are set based on input/output and magnetic coupling parameters, such as operating frequency and the maximum misalignment distance value. Secondly, the three coils are designed according to the study by Li et al. [23]. Thirdly, the resonant network and reconfigurable CC-CV charging topology are designed on the basis of component current and voltage stress and input/output parameters.

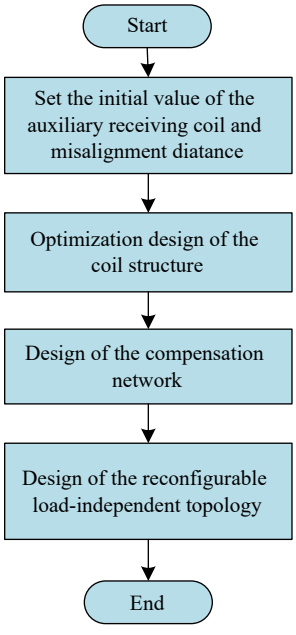

Fig. 11 Flow chart of the proposed IPT system.

Experimental evaluation

Characteristics of the IPT system with a third coil

Initially, a 200 W experimental prototype is built and tested to evaluate its performance, as presented in Fig. 12. According to Tables 1 and 2, the proposed IPT system shows essential characteristics and resonant network parameters, with DSP as the main controller. The air gap is 100 mm on the primary side and secondary side of the coil. The dimensions of the primary coil and secondary coil are 250 mm × 250 mm and 240 mm × 240 mm, respectively. The JMAG simulation model is shown in Fig. 13. The designed dimensional parameters of the proposed third-coil structure are listed in Table 3. In the actual experimental process, the reconfigurable topology and related control circuits are integrated into the secondary side coil in order to further reduce the weight of the receiving side.

Performance of the proposed IPT charger

Figure 13 depicts the magnetic field distribution under alignment and misalignment conditions. In Fig. 14a, the magnetic flux density is displayed when distance is set to 90 mm under the alignment

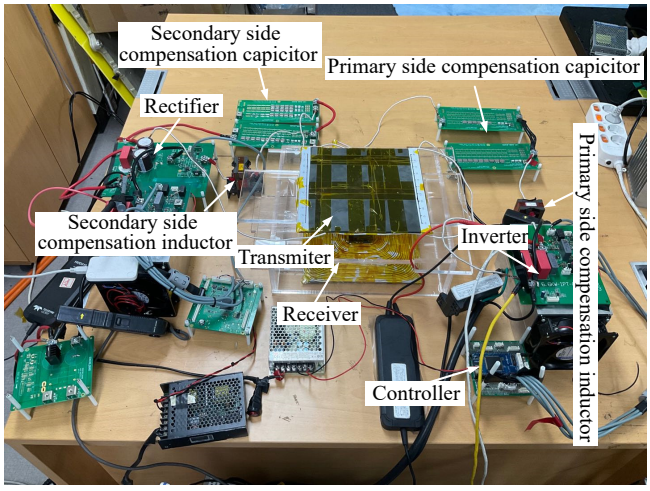

Fig. 12 Experiment setup.

conditions. The proposed third-coil structure design is beneficial to improve the anti-misalignment capability in the horizontal direction. Figure 14b illustrates the magnetic flux density when the receiver undergoes a horizontal movement of 100 mm, while distance remained constant. It is evident from Fig. 14b that the magnetic field density distribution is slightly weakened but remains relatively uniform, indicating that M_{eq} can remain constant after misalignment occurs.

Figure 15 shows the experimental waveform of the input/output voltage and current for the resonant network under the CC condition. The inverter includes a zero phase angle (ZPA) condition which aligns with the theoretical analysis. An example of an experimental waveform of the half-bridge inverter and rectifier under the CC condition is shown. Figure 16 shows the DC output characteristics as the load varies. Apparently, when the DC resistance increases from 18 to 32 Ω, the DC output power rises from 110 to 200 W, the output voltage increases from 44 V to 80 V, and the output current remains 2.5 A. The maximum fluctuation of system output current is 3%.

Figure 17 shows the experimental waveform of the input/output voltage and current for a resonant network under the CV condition. The inverter includes a ZPA condition, which agrees well with the theoretical analysis. The DC output characteristics under load variation are presented in Fig. 18. It indicates that when the DC resistance increases from 36 to 50 Ω, the DC output power decreases from 178 to 128 W, the output current decrease from 2.25 to 1.6 A, the output voltage remains constant to 80 V. The maximum

Table 1. Essential system parameters of proposed IPT system.

Symbols	Parameters	Values
$U_{DC\text{-}link}$	DC-link input voltage	120 V
f_o	Resonant frequency	85 kHz
P_o	Rate output power	200 W
U_o	Battery charging voltage	80 V
I_o	Battery charging current	2.5 A
k	Coupling coefficient	0.073~0.122
L_P	Primary coil inductance	250.9 μH
L_S	Secondary coil	161.1 μH
L_T	Third coil	106.1 μH
M_{PT}	MI between L_P and L_T	16.69 μH
M_{PS}	MI between L_P and L_S	27.85 μH
M_{TS}	MI between L_T and L_S	87.1 μH
R_{Lp}	Transmitting-coil AC resistance of L_p	221.03 mΩ
R_{Ls}	Transmitting-coil AC resistance of L_s	153.26 mΩ
R_{LT}	Receiving-coil AC resistance of L_T	37.75 mΩ
R_{L1}	Resistance of inductance L_1	50.8 mΩ
R_{L2}	Resistance of inductance L_2	62.9 mΩ
R_{Cp1}	Resistance of capacitor C_{p1}	13.3 mΩ
R_{Cp2}	Resistance of capacitor C_{p2}	13.7 mΩ
R_{Cf1}	Resistance of capacitor C_{f1}	5.4 mΩ
R_{Cf2}	Resistance of capacitor C_{f2}	4.8 mΩ
r_{CF}	Turn ON-state resistance of the diodes	4.6 mΩ
$R_{ds(on)}$	The drain-source on-state resistance	39 mΩ

Table 2. Parameters of the resonant network.

Parameter	Value
L_1	16.54 μH
L_2	16.53 μH
C_{P1}	212 nF
C_{f1}	13.97 nF
C_{P2}	212 nF
C_{f2}	45.85 nF

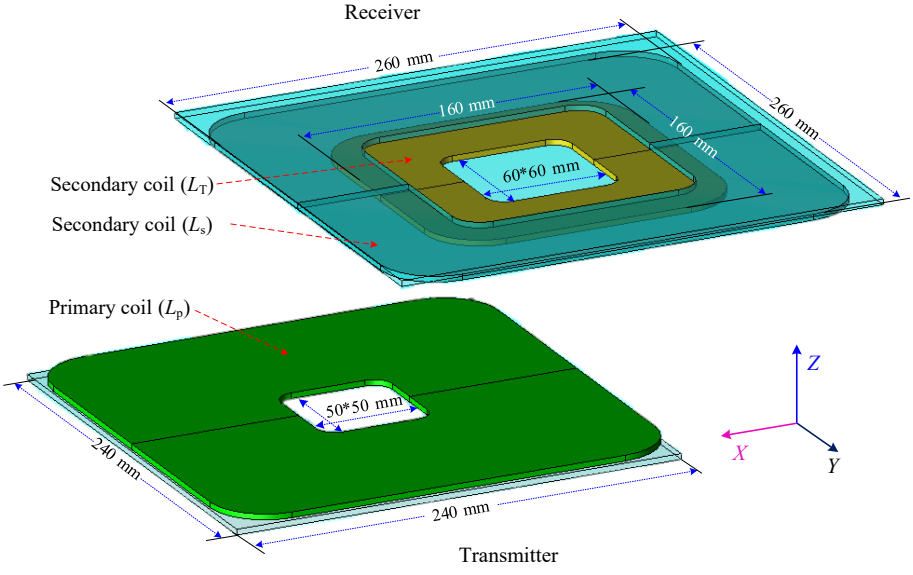

Fig. 13 JMAG simulation model.

Table 3. Essential parameters of the proposed coils.

Symbol	Parameter value	
L_P	Length × width	240 mm × 240 mm
L_T	Length × width	160 mm × 160 mm
L_S	Length × width	250 mm × 250 mm
D_d	Inside radius (L_S)	50 mm
n_P	Turns (L_P)	27
n_S	Turns (L_S)	18
n_T	Turns (L_T)	16
R(P)	Transmitting coil dimension	240 mm × 240 mm × 2.5 mm
R(S)	Receiving coil dimension	250 mm × 240 mm × 5 mm

fluctuation of the system's output current is 2%. In addition, due to the small load resistance value and the single capacitor structure on the secondary side, the AC output current distortion in CV charging mode is smaller than CC charging mode.

Performance of the proposed IPT Charger under the misalignment conditions

Figure 19 shows the input voltage and current waveform of the resonant network and rectifier under the well-aligned and 100 mm misalignment conditions for CC charging process. The findings indicate that the inverter achieves ZVS functionality alongside stable operation of the system. In addition, it can be concluded through experiments that the fluctuation range of the output current under the misalignment state is [−2.3%, 3.2%]. This fluctuation range ensures the stability of the system's current during the actual charging process.

Figure 20 shows the input voltage and current waveform of the resonant network and rectifier under the well-aligned and 100 mm misalignment conditions for CV charging process. Findings indicate that the inverter switches are capable of attaining ZVS, and the system maintains consistent functionality. In addition, it can be concluded through experiments that the fluctuation range of the output voltage under the misalignment state is [−2.5%, 3.7%]. This fluctuation range ensures the stability of the system current during the actual charging process.

A comparison with other methods proposed in the literature is shown in Table 4. A high-reliability three-coil hybrid IPT (Inductive Power Transfer) topology is proposed, which exhibits improved tolerance to coupling variation and provides a load-independent output[24]. This paper has several identified weaknesses: the air gap is relatively small, causing a low coupling coefficient; and to initiate

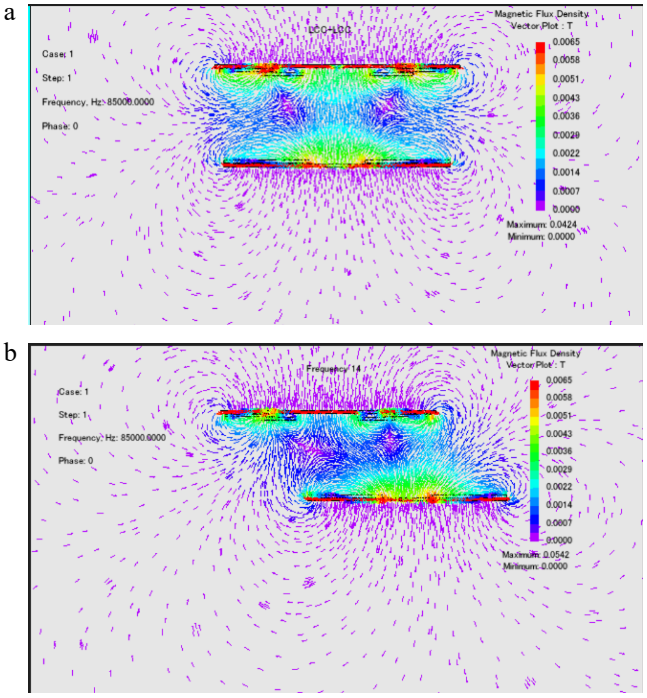

Fig. 14 Simulated magnetic flux density under (a) alignment. (b) X- or Y-axis misalignment with 42% deviation.

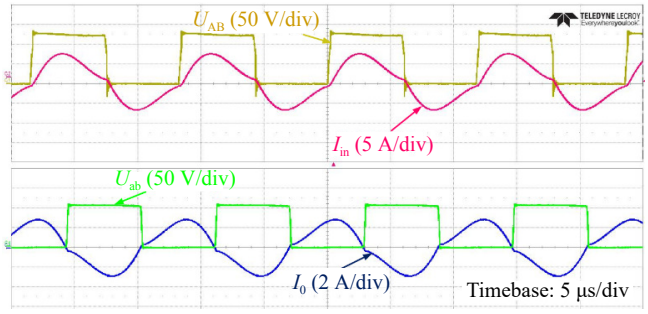

Fig. 15 Experimental waveforms of UAB, Uab, Iin, and Io in the CC mode.

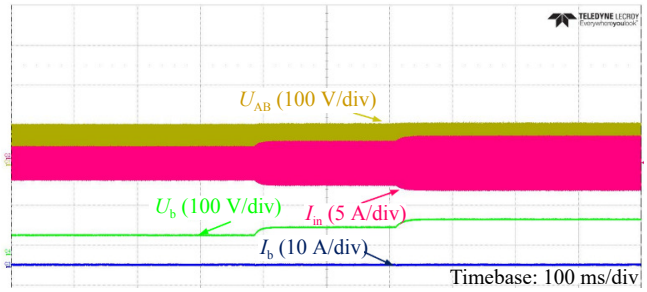

Fig. 16 Experimental waveforms of Ub and Ib in the CC mode with RL varying from 24 to 32 Ω.

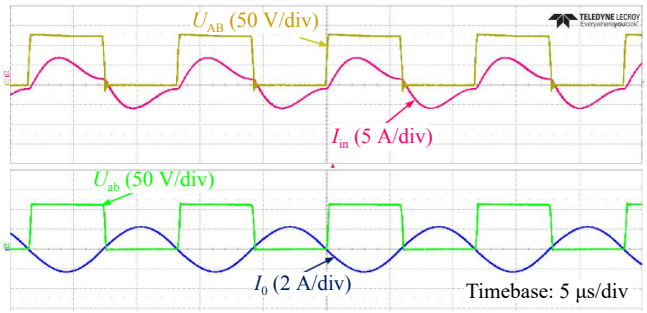

Fig. 17 Experimental waveforms of UAB, Uab, Iin, and Io in the CV mode.

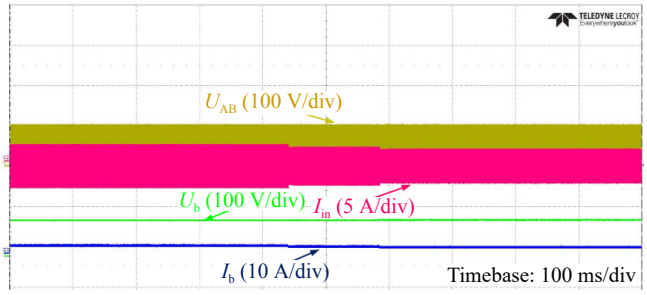

Fig. 18 Experimental waveforms of Ub and Ib in the CV mode with RL varying from 36 to 50 Ω.

Table 4. Comparison with other methods reported in the literature.

Inductor/ capacitor counts	Switch counts	Coils of LCT	Misalignment tolerance X-direction	Misalignment tolerance Y-direction	Output characteristic	Efficiency	Max. power	Ref.
2/6	4	4	37%	37%	CP	85.5%–93.1%	700 W	[23]
1/3	4	3	50%	50%	CC/CV	88.2%–92.5%	460 W	[24]
1/3	4	3	50%	50%	CC	76%–84%	200 W	[25]
4/6	6	4	50%	12.5%	CC/CV	85.7%–93.9%	1 kW	[26]
2/6	4	4	37.5%	37.5%	CV	87%–93.9%	3.5 kW	[27]
1/3	4	2	50%	50%	CV	81%–88%	700 W	[28]
2/4	4	3	40%	40%	CC	92%	3.4 kW	[29]
2/4	4	3	50%	50%	CC	80.6%	100 W	[30]
2/4	4 + 3	3	42%	42%	CC/CV	86.5%–92.9%	200 W	This work

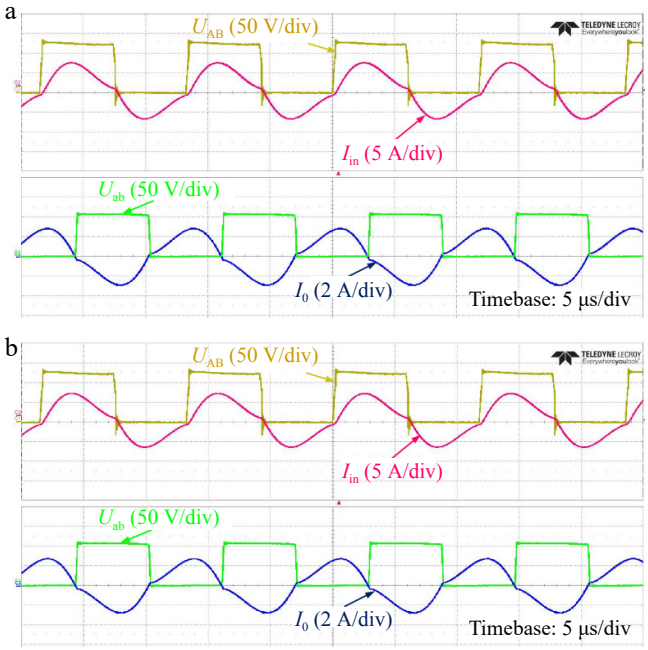

Fig. 19 Experimental waveforms of alignment and misalignment condition in CC mode. (a) Alignment condition. (b) Misalignment condition.

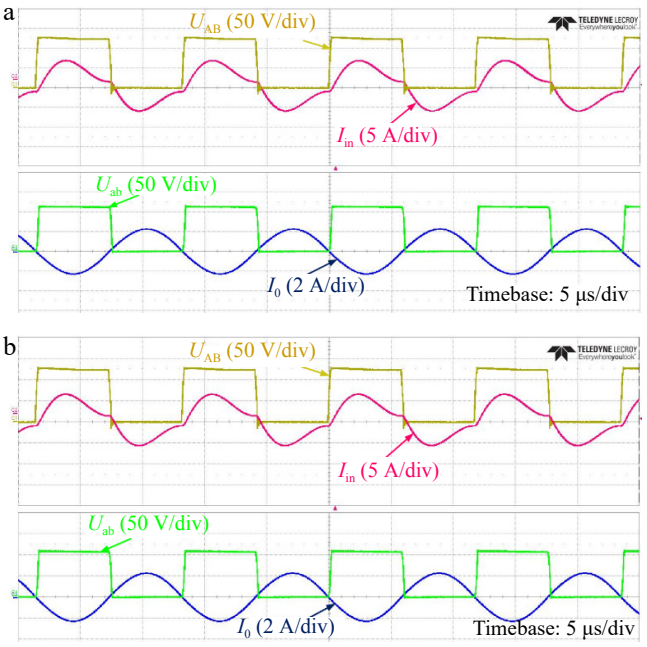

Fig. 20 Experimental waveforms of alignment and misalignment conditions in CV mode. (a) Alignment condition. (b) Misalignment condition.

CC and CV charging, an extra AC switch is necessary, leading to a rise in the system's overall volume and complexity. Primarily, the proposed technique offers an improved balance between the number of components and the features of the output.

A hybrid and reconfigurable system is introduced to achieve high misalignment tolerance while enabling both CC and CV charging capabilities[25]. The system can operate with misalignment to 50% in the x/y direction, with resistance varying from 36 to 480 Ω, and the output fluctuation remains within 5%. However, the coupling relationship of this coil is relatively complex, and the constant output topology utilizes many active components, increasing system volume and losses. Another article introduces an anti-misalignment WPT system based on an LCC-S topology, featuring dual coupled transmitting coils with reverse-parallel windings[26]. The output remains stable under the misalignment condition. However, this system can only achieve CV charging, and the efficiency is low throughout the charging process. Another approach is to significantly enhance tolerance to horizontal misalignment by introducing an anti-series three-coil LCT configuration[27]. Nevertheless, the design encountered several challenges: the AC resistance of the receiving coil was notably increased due to the numerous turns needed to enhance the self-inductance of L_P; adjustments to the air gap D necessitated modifications in coil turns, adding design complexity of the LCT; and the significant misalignment deviation led to fluctuations in the self-inductance of L_P.

In response to the challenges faced by the third coil structure, the LCT designed in this paper uses Litz wire with a higher number of strands to reduce the equivalent series AC resistance of the coil. If the application scenario of the wireless charging system has a tolerance on the air gap D, it can be solved using a control strategy, such as using a buck-boost converter on the primary or secondary side, and applying phase shift control or duty cycle control for the inverter. The dimensions of the third coil structure (L_P : L_S : L_T) are set to 240:250:160 mm, optimizing the misalignment tolerance of the LCT in the horizontal direction. In addition, third coils are introduced on the secondary side to alleviate the impact of self-inductance changes on the current/voltage gain and input phase angle of the system.

Figure 21 depicts the output power and system efficiency according to load variations. The maximum system efficiency of CC and CV charging are 92.23% and 92.27% respectively. The maximum efficiency is 92.27% which appears at 123 W for the proposed IPT system.

Figure 22 illustrates each component's losses and efficiency distribution of the presented system. Losses in the system can be quantified using a power analyzer, and the detailed distribution of losses

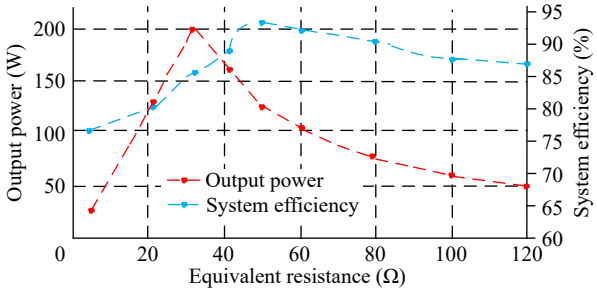

Fig. 21 Efficiency and output power of the proposed IPT system.

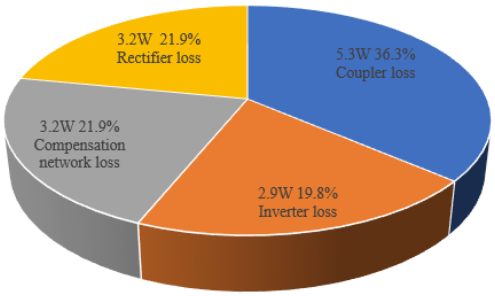

Fig. 22 Efficiency distribution of the proposed IPT system.

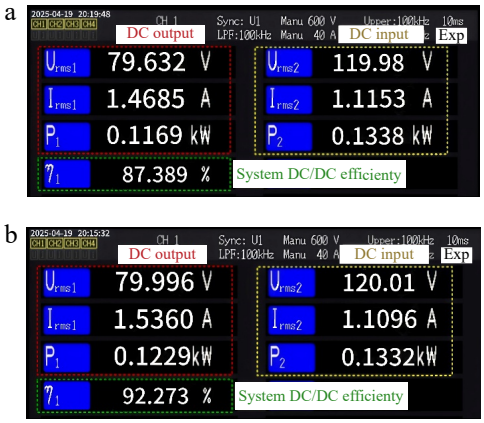

Fig. 23 Power analyzer data in the CV mode. (a) Misaligned state. (b) Aligned state.

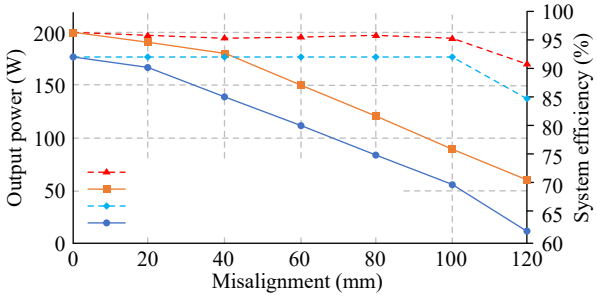

Fig. 24 Output power and efficiency comparison between third-coil and two-coil coupler with misalignment.

for each component can be inferred through computational techniques. A power analyzer measures the overall losses and current/voltage amplitudes, followed by a comprehensive calculation of the loss distribution based on the measured currents and voltages[28]. Furthermore, to enhance the accuracy of the loss distribution, core losses were simulated using finite element method simulations[29,30]. Due to the ZVS operation of the power switching device, inverter losses account for a relatively small proportion of the total. The test outcomes reveal that the majority of system losses originate from the coupler.

Figure 23 illustrates the waveforms captured by the power analyzer under constant voltage (CV) mode, demonstrating a system efficiency of 92.27%. Analysis of the efficiency reveals that the suggested network structure significantly enhances the system's effectiveness.

Figure 24 illustrates the performance comparison between the proposed three-coil magnetic coupler and the traditional two-coil configuration under misalignment conditions. The results indicate a substantial decline in both output power and system efficiency for the two-coil structure when misaligned. The analysis confirms that the three-coil design offers improved practicality and effectiveness.

Conclusions

This paper presents a high-performance wireless charging topology structure that incorporates a third-coil loosely coupled transformer to improve the system's misalignment performance, and utilizes a reconfigurable topology structure to achieve constant current and voltage output. The maximum deviation of the coil in the x and y directions can reach 42%, and the maximum transmission efficiency is 92.27%. This structure does not require communication between the main and ancillary sides and utilizes fewer active components to achieve a higher power density.

Author contributions

The authors confirm their contribution to the paper as follows: Study conception and design: Zhang H, Zhou X; data collection: Zhang H, Tian S; analysis and interpretation of results: Zhang H, Tian S, Wang H; draft manuscript preparation: Zhang, Tian S, Wang H, Zhou X. All authors reviewed the results and approved the final version of the manuscript.

Data availability

The data generated or analyzed during the current study are included in this published article and are available from the corresponding author upon reasonable request.

Acknowledgments

This work was supported in part by the Natural Science Foundation of Shangdong Province (Grant No. ZR2022ME214).

Conflict of interest

The authors declare that they have no conflict of interest.

Dates

Received 23 December 2024; Revised 21 April 2025; Accepted 28 April 2025; Published online 7 July 2025

References

1. Feng H, Cai T, Duan S, Zhang X, Hu H, et al. 2018. A dual-side-detuned series–series compensated resonant converter for wide charging region in a wireless power transfer system. *IEEE Transactions on Industrial Electronics* 65:2177–88
2. Zhao J, Cai T, Duan S, Feng H, Chen C, et al. 2016. A general design method of primary compensation network for dynamic WPT system maintaining stable transmission power. *IEEE Transactions on Power Electronics* 31:8343–58

3. Yao Y, Wang Y, Liu X, Lu K, Xu D. 2018. Analysis and design of an S/SP compensated IPT system to minimize output voltage fluctuation versus coupling coefficient and load variation. *IEEE Transactions on Vehicular Technology* 67:9262–72
4. Hou J, Chen Q, Zhang Z, Wong SC, Tse CK. 2018. Analysis of output current characteristics for higher order primary compensation in inductive power transfer systems. *IEEE Transactions on Power Electronics* 33:6807–21
5. Feng H, Dayerizadeh A, Lukic SM. 2021. A coupling-insensitive X-type IPT system for high position tolerance. *IEEE Transactions on Industrial Electronics* 68:6917–26
6. Wu HH, Gilchrist A, Sealy KD, Bronson D. 2012. A high efficiency 5 kW inductive charger for EVs using dual side control. *IEEE Transactions on Industrial Informatics* 8:585–95
7. Sample AP, Waters BH, Wisdom ST, Smith JR. 2013. Enabling seamless wireless power delivery in dynamic environments. *Proceedings of the IEEE* 101:1343–58
8. Miller JM, Onar OC, Chinthavali M. 2015. Primary-side power flow control of wireless power transfer for electric vehicle charging. *IEEE Journal of Emerging and Selected Topics in Power Electronics* 3:147–62
9. Chen Y, Yang B, Zhou X, Li Q, He Z, et al. 2020. A hybrid inductive power transfer system with misalignment tolerance using quadruple-D quadrature pads. *IEEE Transactions on Power Electronics* 35:6039–49
10. Zaheer A, Hao H, Covic GA, Kacprzak D. 2015. Investigation of multiple decoupled coil primary pad topologies in lumped IPT systems for interoperable electric vehicle charging. *IEEE Transactions on Power Electronics* 30:1937–55
11. Kim S, Covic GA, Boys JT. 2017. Tripolar pad for inductive power transfer systems for EV charging. *IEEE Transactions on Power Electronics* 32:5045–57
12. Zheng C, Ma H, Lai JS, Zhang L. 2015. Design considerations to reduce gap variation and misalignment effects for the inductive power transfer system. *IEEE Transactions on Power Electronics* 30:6108–19
13. Li G, Ma H. 2022. A hybrid IPT system with high-misalignment tolerance and inherent CC–CV output characteristics for EVs charging applications. *IEEE Journal of Emerging and Selected Topics in Power Electronics* 10:3152–60
14. Budhia M, Boys JT, Covic GA, Huang CY. 2013. Development of a single-sided flux magnetic coupler for electric vehicle IPT charging systems. *IEEE Transactions on Industrial Electronics* 60:318–28
15. Li Y, Lin T, Mai R, Huang L, He Z. 2018. Compact double-sided decoupled coils-based WPT systems for high-power applications: analysis, design, and experimental verification. *IEEE Transactions on Transportation Electrification* 4:64–75
16. Fu M, Ma C, Zhu X. 2014. A cascaded boost–buck converter for high-efficiency wireless power transfer systems. *IEEE Transactions on Industrial Informatics* 10:1972–80
17. Li H, Li J, Wang K, Chen W, Yang X. 2015. A maximum efficiency point tracking control scheme for wireless power transfer systems using magnetic resonant coupling. *IEEE Transactions on Power Electronics* 30:3998–4008
18. Liu Y, Madawala UK, Mai R, He Z. 2020. Zero-phase-angle controlled bidirectional wireless EV charging systems for large coil misalignments. *IEEE Transactions on Power Electronics* 35:5343–53
19. Liu Y, Madawala UK, Mai R, He Z. 2020. An optimal multivariable control strategy for inductive power transfer systems to improve efficiency. *IEEE Transactions on Power Electronics* 35:8998–9010
20. Sample AP, Meyer DT, Smith JR. 2011. Analysis, experimental results, and range adaptation of magnetically coupled resonators for wireless power transfer. *IEEE Transactions on Industrial Electronics* 58:544–54
21. Zhang Z, Zheng S, Luo S, Xu D, Krein PT, et al. 2022. An inductive power transfer charging system with a multiband frequency tracking control for misalignment tolerance. *IEEE Transactions on Power Electronics* 37:11342–55
22. Chen Y, He S, Yang B, Chen S, He Z, et al. 2023. Reconfigurable rectifier-based detuned series-series compensated IPT system for anti-misalignment and efficiency improvement. *IEEE Transactions on Power Electronics* 38:2720–29
23. Li H, Liu M, Kong L, Wang Y. 2023. An independent dual-coil driving topology for wireless power transfer. *IEEE Transactions on Power Electronics* 38:1378–83
24. Wang Y, Liu H, Wu F, Wheeler P, Zhou Q, et al. 2023. Research on a three-coil hybrid IPT charger with improved tolerance to coupling variation and load-independent output. *IEEE Journal of Emerging and Selected Topics in Industrial Electronics* 4:625–36
25. Yuan Z, Saeedifard M, Cai C, Yang Q, Zhang P, et al. 2022. A misalignment tolerant design for a dual-coupled LCC-S-compensated WPT system with load-independent CC output. *IEEE Transactions on Power Electronics* 37:7480–92
26. Wu Y, Liu C, Zhou M, Mao X, Zhang Y. 2023. An antioffset electric vehicle wireless charging system based on dual coupled antiparallel coils. *IEEE Transactions on Power Electronics* 38:5634–37
27. Chen Y, Mai R, Zhang Y, Li M, He Z. 2019. Improving misalignment tolerance for IPT system using a third-coil. *IEEE Transactions on Power Electronics* 34:3009–13
28. Ramezani A, Farhangi S, Iman-Eini H, Farhangi B, Rahimi R, et al. 2019. Optimized LCC-series compensated resonant network for stationary wireless EV chargers. *IEEE Transactions on Industrial Electronics* 66:2756–65
29. Chen Y, Zhang H, Shin CS, Jo CH, Park SJ, et al. 2020. An efficiency optimization-based asymmetric tuning method of double-sided LCC compensated WPT system for electric vehicles. *IEEE Transactions on Power Electronics* 35:11475–87
30. Wojda RP, Kazimierczuk MK. 2012. Winding resistance of litz-wire and multi-strand inductors. *IET Power Electronics* 5:257–68